PROTOTYPE OF PROBABILISTIC AVALANCHE HAZARD MAP REFLECTING UNCERTAINTIES OF SNOW COVER CONDITIONS DURING WINTER

Takahiro Tanabe[1]*, Sojiro Sunako[2], and Kouichi Nishimura[3]

[1] *National Research Institute for Earth Science and Disaster Resilience, Yamagata, Japan*
[2] *National Research Institute for Earth Science and Disaster Resilience, Niigata, Japan*
[3] *Professor emeritus of Nagoya University, Aichi, Japan*

ABSTRACT: Snow avalanches are natural disasters that occur in snowy mountainous regions, threatening settlements and their inhabitants. Hence, a hazard map is a means of mitigating their impact. Avalanche flow models have been employed to indicate avalanche runout areas. These models require inputs, such as the digital elevation model, release area, initial conditions, and model parameters. Although the dynamics of the models depend on the input values, they are generally uncertain. In this study, we considered three uncertain input variables: the initial flow thickness, friction coefficient, and drag coefficient, whereas the other input variables were set to constant values. Additionally, we assumed that the uncertainties in the input variables could be represented by probability density distributions and combined them with flow models to generate probabilistic hazard maps. In this study, probability refers to the exceedance probability that the output of the flow model, such as the maximum flow thickness, exceeds a given threshold value. To evaluate the uncertainties, we used the Polynomial Chaos Quadrature method and prototyped probabilistic avalanche hazard maps using the following procedure: Potential Release Areas (PRAs) were identified on a specific slope in Japan. Assuming lower and upper bounds for each uncertain input variable of the flow model, we created a probabilistic hazard map for avalanches at a specific PRA. Two scenarios for uncertain input distributions are considered: uniform and Gaussian distributions. The uniform distribution case indicates superimposing potential avalanches on the PRA, and the Gaussian distributions were determined to reflect actual snow conditions, such as snow depth and snow wetness, which update the uncertain distributions. The necessity of reflecting snow conditions was confirmed by comparing the hazard maps. Additionally, by reflecting snow conditions, the runout areas of past avalanche events can be reproduced. These probabilistic hazard assessments led to quantitative risk evaluations, which will be the focus of future work.

KEYWORDS: Probabilistic hazard map; Uncertainty quantification; Hazard assessment; Risk assessment

1. INTRODUCTION

Snow avalanches are common disasters which threaten inhabitants of snowy regions. Consequently, various studies have been conducted to understand statistical laws and flow dynamics (McClung and Schaerer, 2006). Avalanche hazard maps were created to mitigate avalanche damage.

One of famous avalanche zoning methods is the $\alpha - \beta$ model, which uses topographic angles and their statistical relationship (Bakkehøi et al., 1983). Avalanche zoning using topographic angles was combined with GIS analysis to create nationwide hazard indication maps (Derron and Sletten, 2016). Although analysis using topographic angles is simple, applying this method requires assumptions about the path and horizontal propagation. Hazard maps based on flow models that do not require such assumptions have also been developed (Barbolini and Savi, 2001; Jamieson et al., 2008; Bühler et al., 2018, 2022). For instance, the hazard map proposed by Issler et al. (2023) reported the runout areas of historical scale avalanche, which yielded better results than zoning based on the $\alpha - \beta$ model. This highlights the importance of flow models in hazard mapping.

To create hazard maps using flow models, it is necessary to set input values, such as the digital elevation model (DEM), avalanche release area, initial conditions, and model parameters. Therefore, in hazard maps with flow models, the estimation of potential release areas (PRAs), which are used for the release areas of the models, is first performed by combining topography, vegetation, and artificial anti-avalanche countermeasures (Bühler et al., 2022; Issler et al., 2023). For the estimated PRAs, a set of initial conditions and model parameters was provided considering the meteorological characteristics of the region. A flow model is used to illustrate the avalanche runout area. In previous studies, simulations were

* *Corresponding author address:*
Takahiro Tanabe, National Research Institute for Earth Science and Disaster Resilience, Snow and Ice Research Center, 1400 Tokamachi, Shinjo, Yamagata, Japan;

tel: ++81 233 23 8003;
email: tnabe@bosai.go.jp

performed using a typical set of model input values for the specific situations (Issler et al., 2023).

However, there is uncertainty in the input variables of avalanche models. For example, Fischer et al. (2015, 2020) demonstrated that the optimal model parameters that reproduced documented avalanche events were not a set of specific values but were obtained as distributions. The distributions arise from errors in the observations, numerical calculations, and modeling. The uncertainties in the input variables propagate to the output through model calculations. By quantifying the input uncertainty, known as uncertainty quantification, runout areas have been illustrated with exceedance probabilities (Dalbey et al., 2008; Tierz et al., 2019; Tanabe et al., 2024). A probabilistic hazard map (PHM) shows the spatial distribution of the exceedance probability, which indicates that the output values from the flow model, such as the flow thickness or pressure, exceed a given threshold. As risk is calculated as the product of hazard, vulnerability, and exposure, this probabilistic disaster assessment is related to risk assessment (Ortner et al., 2023). Thus, a quantitative evaluation of the uncertainty in the input variables for flow models is expected to enhance decision making for avalanche disaster countermeasures.

This study aimed to create a prototype avalanche PHM for a specific location in Japan using the method proposed by Tanabe et al. (2024), in which two types of PHMs were proposed using the polynomial chaos quadrature (PCQ) method: one that considers all potential parameter ranges during the snow season via a uniform distribution of input variables, and another that reflects current snow conditions whose uncertainties can be expressed by non-uniform distributions. In their method, the latter map could be generated at lower computational costs. In this study, we show the PHMs for situations reflecting three different snow cover conditions: early winter, mid-winter, and late winter. We assumed that each situation had different snow conditions. Snow is a relatively small amount of dry, slippery snow at the beginning of winter, becomes a large amount of wet snow in mid-winter, and finally becomes wet, less slippery snow during the melting period.

To achieve PHMs that reflect snow conditions, PRAs is first estimated for the target area, and the potential range of input values that can be considered under PRA is determined. Assuming that each uncertain input variable independently follows a uniform distribution, the PCQ method is implemented to draw a PHM for the uniform distribution case, and an emulator functioning within the initial parameter ranges is created. Subsequently, a hazard map is generated for cases in which the distributions of the input values are non-uniform.

2. MATERIALS AND METHODS

2.1 *Target Area for Hazard Mapping*

The target area for creating the hazard maps in this study was Route 112 (R112) in Yamagata Prefecture, Japan, named Gassan Road (Fig. 1). This road is an important logistics route connecting the inland and coastal areas of the region at a distance of 30.9 km. This road crosses mountains exceeding 2,000 m in elevation, with the highest elevation on the road being 734 m and the maximum gradient of the road being approximately 5%. A digital elevation model (DEM) for this area was obtained from the Geospatial Information Authority of Japan with a 10-m grid size.

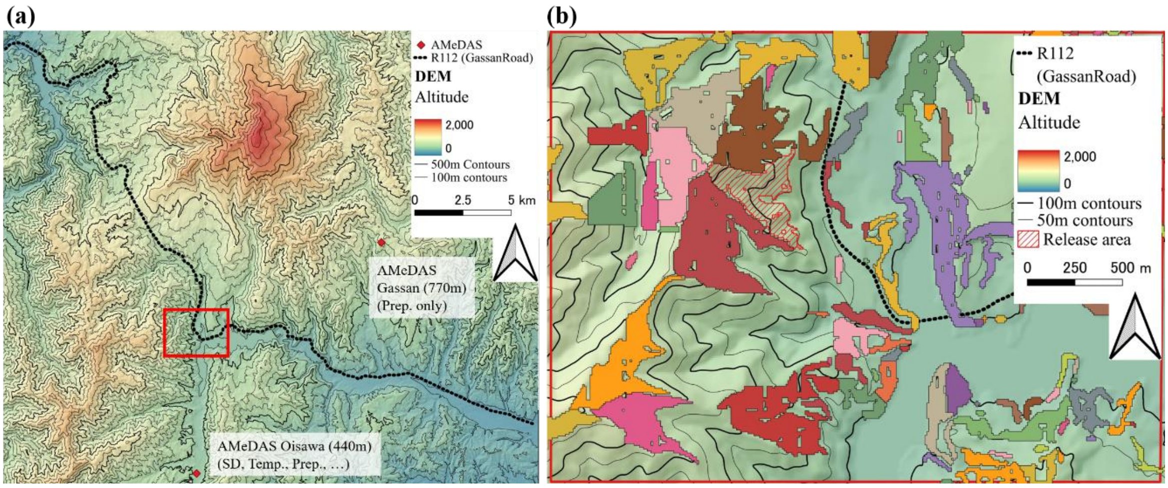

Figure 1: (a) Target region and Gassan road. The colors and contour lines represent elevation. The diamonds indicate AMeDAS locations, with place name, elevation, and measured items. (b) Enlarged view within the square shown in (a). Polygons indicate potential release areas (PRAs). The hatched polygon is the release area used in this study and filled polygons are PRAs estimated in Section 2.2.

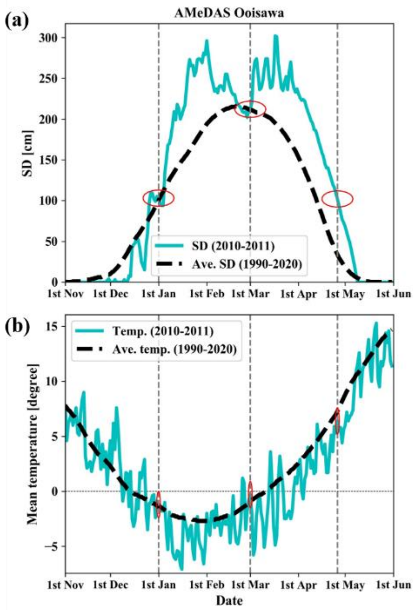

Figure 2: (a) Snow depth and (b) daily average temperature at the Oisawa AMeDAS. The dashed line represents the average values from 1990 to 2020, while the solid line represents the 2010-2011 winter season. Red circles correspond to the early, mid-, and late winter of the season.

There is a weather station close to the road, named the Oisawa Automated Meteorological Data Acquisition (AMeDAS), which is maintained by the Japan Meteorological Agency (Fig. 1(a)). The Oisawa AMeDAS is located on flat land at 440 m a.s.l. and measures the snow depth, temperature, and precipitation. Figure 2 shows the snow depth and daily average temperature for an average year and the 2010-2011 winter. On average, snow depth reached a maximum value of 200 cm from late February to early March (Fig. 2(a)). At the Oisawa AMeDAS, the maximum snow depth during 1980-2024 was 3.5 m.

Road R112 has experienced closure due to avalanches in the past. Here, we focus on the full-depth snow avalanche that occurred on February 27th, 2011. In this event, no vehicles were caught; however, a full road closure was enforced for one week, followed by a night-time closure for an additional two weeks. According to an investigation by Abe et al. (2012), the snow depth in the release area was estimated to be over 2 m, consisting mainly of granular snow with a snowpack density on the avalanche slope of 400 kg/m^3. The avalanche release point was located approximately 8 km north of the Oisawa AMeDAS, and the elevation at the avalanche point was approximately 570 m. In Section 3.3, the validation for this event is described.

2.2 Avalanche Potential Release Areas

The PRAs have been estimated for avalanches (Gauer 2018; Bühler et al., 2018, 2022; Issler et al., 2023). PRAs estimation in this study was conducted by referring to previous studies.

To detect the PRAs, the slope angle of the target area was considered. In this study, areas where the slope angle was within the range of 20°-50° were extracted. This range is slightly different from the slope angles used in previous studies, for example, 30°-55° by Issler et al. (2023). These differences are thought to arise from the topographical features, vegetations, and avalanche scales of the areas where the PRAs are determined.

Next, to limit the avalanche release areas, the areas extracted based on the slope angles were divided into catchments. To detect the release areas from the divided regions, the upper part of each area was only considered when there was an elevation difference of ≥ 200 m. Finally, areas larger than 400 m^2 were set as PRAs and areas less than the given threshold were ignored. Although this procedure followed the method reported by Issler et al. (2023) without forests, the threshold values were adapted for Japan. For further improvements, modifications based on the statistical analysis of past avalanche events in Japan are essential.

2.3 Probabilistic Hazard Map with Polynomial Chaos Quadrature method

For each PRA, uncertainty quantification was conducted using appropriate input value ranges. Although the Monte Carlo (MC) method is well-known for uncertainty quantification, this study used the PCQ method. PCQ shows faster conversion than MC when the number of uncertainty variables is small (Dalbey et al., 2008; Tanabe et al., 2024).

The PCQ consists of three steps. The first step is the polynomial chaos (PC) expansion proposed by Weiner (1938) and generalized by Xiu and Karniadakis (2002). The second step is the derivation of the PC coefficients using a Gaussian quadrature. The third step is to calculate the exceedance probability using the obtained polynomial with secondary sampling points (SSPs) to create a hazard map.

Following Tanabe et al. (2024), we first consider the case where uncertainty is represented by uniform distributions. Let $\boldsymbol{\theta} = (\theta_1, \cdots, \theta_D)$ be the uncertain input values, and $y = y(\boldsymbol{\theta}, \boldsymbol{x})$ be a simulation output using uncertain input $\boldsymbol{\theta}$ at each location $\boldsymbol{x}$, such as maximum flow thickness and maximum flow velocity. Each input variable θ_d individually follows the uniform distribution as $\theta_d \sim U(\theta_{min}^d, \theta_{max}^d)$ $(d = 1, \cdots, D)$. The upper and lower bounds, θ_{max} and θ_{min} respectively, are set to include the potential parameter range in the PRA.

The PC expansion, considering truncation up to K is expressed as follows:

$$y(\boldsymbol{\theta},\boldsymbol{x}) \approx y_K(\boldsymbol{\theta},\boldsymbol{x}) = \sum_{k=0}^{K} b_k(\boldsymbol{x})\Phi_k(\boldsymbol{\xi_\theta}), \qquad (1)$$

where, $b_k(\boldsymbol{x})$ is the k-th coefficient at location $\boldsymbol{x}$, Φ_k is the k-th orthogonal polynomial, and $\boldsymbol{\xi_\theta} = (\xi_1,\cdots,\xi_D)$ are variables of $\xi_d \in [-1,1]$. ξ corresponds to the input variable θ through the following transformation: $\theta = \theta_{sum} + \theta_{diff}\xi$, where $\theta_{diff} = \frac{1}{2}(\theta_{max} - \theta_{min})$, $\theta_{sum} = \frac{1}{2}(\theta_{max} + \theta_{min})$.

If $D = 1$, the basal orthogonal polynomial Φ_k for a uniform distribution is the Legendre polynomial Le_k (Xiu and Karniadakis, 2002). For $D \geq 2$, Φ_k is expressed as the product of Legendre polynomials (Sullivan, 2015). The truncation K corresponds to the maximum degree of the polynomial N_P for $D = 1$, and is given by $K = (N_P + D)!/(N_P!\,D!)$ for $D \geq 2$ (Sullivan, 2015).

Since Φ_i is mutually orthogonal, the inner product $\langle\cdot,\cdot\rangle$ can be calculated as $\langle\Phi_i,\Phi_j\rangle = \int \Phi_i\Phi_j W d\boldsymbol{\xi} = \lambda_i\delta_{ij}$, where $W(\boldsymbol{\xi})$ is the weight function, δ_{ij} is the Kronecker delta, and $\lambda_i = \langle\Phi_i^2\rangle$. For Legendre polynomials, $W(\boldsymbol{\xi}) = 1$ and $\lambda_i = \langle\mathrm{Le}_i^2\rangle = 1/(2i+1)$. To determine the PC coefficients b_k, we take the inner product with Φ_i on both sides of Eq. (1), and the orthogonality yields

$$b_k(\boldsymbol{x}) \approx \frac{1}{\lambda_k}\int \Phi_k(\boldsymbol{\xi})y(\boldsymbol{\theta},\boldsymbol{x})d\boldsymbol{\xi}.$$

Because the integrand is a polynomial, we used the Gaussian quadrature method to obtain

$$b_k(\boldsymbol{x}) \approx \frac{1}{\lambda_k}\sum_{j=1}^{N_Q} q_j\Phi_k(\boldsymbol{\xi}_j)y(\boldsymbol{\theta}_j,\boldsymbol{x}), \qquad (2)$$

where, $\boldsymbol{\xi}_j$ is the j-th nodes and q_j is the j-th weights for the Gaussian quadrature. The coefficients $b_k(\boldsymbol{x})$ are obtained by N_Q simulation iterations $y(\boldsymbol{\theta}_j,\boldsymbol{x})$ using the input values $\boldsymbol{\theta}_j$ that corresponds to $\boldsymbol{\xi}_j$ for $j = 1,\cdots,N_Q$.

The polynomial Eq. (1) was then applied to the SSPs. SSPs $\boldsymbol{\xi}_l = (\xi_1^l,\cdots,\xi_D^l)$ are variables defined in $\boldsymbol{\xi}_l \in [-1,1]^D$ and are used to evaluate the polynomial obtained from Eqs. (1) and (2) as an emulator ($l = 1,\cdots,N_{SSP}$). The exceedance probability $p(y > y_{cri};\boldsymbol{x})$ is then expressed as

$$p(y > y_{cri};\boldsymbol{x}) = \frac{\#(\sum_{k=0}^{K} b_k(\boldsymbol{x})\Phi_k(\boldsymbol{\xi}_l) > y_{cri})}{N_{SSP}}, \quad (3)$$

with the number of SSPs N_{SSP} and a given threshold y_{cri}. The computation of Eq. (1) involves only algebraic calculations and can be performed using matrix operations, resulting in significantly lower computational costs compared to numerical simulations.

2.4 Simulator

In this study, we used the open-source application faSavageHutterFOAM proposed by Rauter et al. (2018). faSavageHutterFOAM solves the mass-conservation equation for flow thickness $h(t,\boldsymbol{x})$, as well as the momentum conservation equations for the slope-tangential and slope-normal directions, to calculate the time evolution of $h(t,\boldsymbol{x})$, the flow velocity $\overline{\boldsymbol{v}}(t,\boldsymbol{x})$, and the basal pressure $p_b(t,\boldsymbol{x})$ at time t and point $\boldsymbol{x}$ as a module of OpenFOAM. The conservation laws are expressed as follows.

$$\frac{\partial h}{\partial t} + \nabla\cdot(h\overline{\boldsymbol{u}}) = 0,$$

$$\frac{\partial}{\partial t}(h\overline{\boldsymbol{u}}) + \nabla_s\cdot(h\overline{\boldsymbol{u}}\overline{\boldsymbol{u}}) = -\frac{1}{\rho}\boldsymbol{\tau}_b + h\boldsymbol{g}_s - \frac{1}{2\rho}\nabla_s(hp_b),$$

$$\nabla_n\cdot(h\overline{\boldsymbol{u}}\overline{\boldsymbol{u}}) = h\boldsymbol{g}_n - \frac{1}{2\rho}\nabla_n(hp_b) - \frac{1}{\rho}\boldsymbol{n}_b p_b,$$

where ρ is density, $\boldsymbol{g}$ and ∇ are the gravitational acceleration and differential operator, respectively, whose subsets s and n indicate the surface-tangential and surface-normal directions, respectively. In addition to the conservation equations, we assume the Voellmy-type basal friction model $\boldsymbol{\tau}_b$ as

$$\boldsymbol{\tau}_b = \mu p_b\frac{\overline{\boldsymbol{u}}}{|\overline{\boldsymbol{u}}| + u_0} + \frac{\rho|\boldsymbol{g}|}{\xi_{drag}}|\overline{\boldsymbol{u}}|\overline{\boldsymbol{u}},$$

with the friction coefficient μ and drag coefficient ξ_{drag}, and tiny constant $u_0 \ll 1$. The simulator solves these equations with the finite area method, constraining the finite volume method to the surface mesh (Rauter and Tuković, 2018).

2.5 Numerical Setting

To perform faSavegeHutterFOAM, the topography DEM (Sect. 2.1), release area S_{rel} and four input variables (initial thickness h_0, ρ, μ, and ξ_{drag}) are required. The area S_{rel} was provided by PRA. Previous sensitivity analysis studies have reported that the influential inputs for flow thickness are h_0, μ, and ξ_{drag} in this order, and ξ_{drag}, h_0, and μ for flow velocity (Fischer et al., 2015; Heredia et al., 2021). Therefore, this study considers the uncertainties of three input variables: h_0, μ, and ξ_{drag}. For density ρ, we set 350 kg/m³, which is an intermediate value between dry and wet snow. The simulation output for PHM in this study is the maximum flow thickness during each simulation: $y(\boldsymbol{\theta},\boldsymbol{x}) = h_{max}(\boldsymbol{\theta};\,\boldsymbol{x}) =$

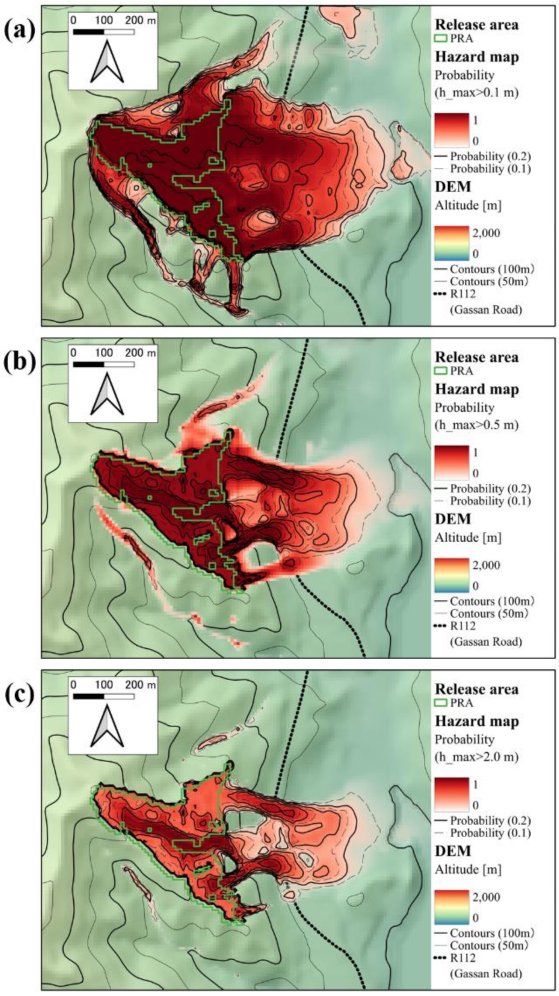

Figure 3: Probabilistic avalanche hazard maps assuming uniform distributions of inputs. The colors represent the exceedance probability of the maximum flow thickness for thresholds of (a) 0.1 m, (b) 0.5 m, and (c) 2.0 m.

$\max_{t \in T} h(t, \boldsymbol{x}, \boldsymbol{\theta})$, where T is the set of simulation output times.

For the uncertainty quantification, the lower and upper bounds of the potential input values must be determined. The initial flow thickness h_0 was determined from the maximum snow depth 3.5 m recorded at the Oisawa AMeDAS, which was increased by factors of 1.5, $[0.2, 5.2]$. The friction coefficient μ and the drag coefficient ξ_{drag} were determined to include values for both dry and wet snow avalanches, as $[0.2, 0.5]$ and $[2000, 30000]$, respectively. To perform PCQ, appropriate settings of N_P, N_Q, and N_{SSP} were required to be effective; $(N_P, N_Q, N_{SSP}) = (8, 8^3, 40^3)$ were employed in this study following Tanabe et al. (2024).

3. RESULTS AND DISCUSSION

3.1 Potential release areas

Figure 1(b) shows the specific PRA obtained using the procedure described in Section 2.2. Within 3.2×2.3 km^2 regions shown in Fig. 1(b), more than 50 PRAs were identified. The specific PRA includes the release area of the past avalanche event, as introduced in Section 2.1.

The PRA shown in Fig. 1(b) considers only topographical conditions. However, tall trees or snow-supporting structures on actual slopes prevent avalanche release. For future development, it will be necessary to consider these effects and exclude areas where avalanches rarely occur.

3.2 Probabilistic Hazard Map with Uncertain Inputs for Uniform Distributions

Figure 3(a)–(c) show the PHMs obtained for the uniform distribution case, $h_0 \sim U(0.2, 5.2)$, $\mu \sim U(0.2, 0.5)$, and $\xi \sim U(2000, 30000)$, with colors representing the exceedance probability for the thresholds $y_{cri} = 0.1, 0.5, 2.0$ m, respectively. Owing to the large size of the PRA, the probability values were close to 1 in areas near the release area and decreased as the distance from the release area increased. This trend remained consistent even when the threshold h_{cir} was changed. However, with a lower threshold ($h_{cir} = 0.1$ m), most areas turned red, whereas with a higher threshold ($h_{cir} = 2.0$ m), the probability decreased sharply with increasing distance.

The uniform distributions considered for creating the PHM consider the potential range of input variables that can occur during winter. In other words, this figure superimposes all outputs obtained from the potential parameters throughout the winter season, thus indicating the avalanche threat that could occur during winter. However, this figure might overestimate or underestimate the actual conditions on a specific winter day. For example, the probability shown in Fig. 3 may be overestimated for early winter because the typical amount of snow for the situation is less than that considered in the figure. Therefore, in the following section, we develop a PHM that reflects these specific conditions.

3.3 Probabilistic Hazard Map with Uncertain Inputs Reflecting Snow Pack Conditions

When changing the input value distributions, recomputation is unavoidable for accurately quantifying the input uncertainty. In the MC method, new input values must be generated based on new probability distributions, necessitating re-simulation. However, in the PCQ method, Eq. (1), which is derived for uniform distributions, can be used as an emulator. By selecting the SSPs according to new probability distributions and using algebraic re-calculations, the input uncertainty can be evaluated, thus significantly reducing the required computational cost. We created PHMs for three situations during the 2010-2011 winter season, roughly corresponding to the early winter, mid-winter, and late winter, which corresponded to the red circles in Fig. 2.

Figure 2 shows the snow depth and daily mean temperature observed at the Oisawa AMeDAS during 2010-2011 winter. The probability distributions of the initial snow thickness h_0 and friction coefficient μ for each period were determined using the observed values. Let us assume that the uncertain values are represented by the Gaussian distribution $\mathcal{N}(m, s^2)$ with mean m and variance s^2, supported within the finite range of the respective original uniform distributions. The mean values for h_0 were obtained based on the observed values. The mean values of μ were typical values for surface avalanches for early winter (mean temperature below 0 °C) and for full-depth avalanches for the remaining two periods (that above 0° C). Variance was determined by considering the reliability of the given mean values. For ξ_{drag}, since its impact on flow thickness is relatively smaller than h_0 and μ (Heredia et al., 2021), it was left as a uniform distribution. Distributions, assuming a representation of the uncertainty, are summarized in Table 1 and illustrated in Fig. 4.

Table 1: Input distributions representing the uncertainty.

	Early-winter	Mid-winter	Late-winter
h_0	$N(1.5, 0.2^2)$	$N(2.0, 0.3^2)$	$N(1.5, 0.2^2)$
μ	$N(0.26, 0.01^2)$	$N(0.425, 0.018^2)$	$N(0.425, 0.018^2)$
ξ_{drag}	$U(2000, 30000)$	$U(2000, 30000)$	$U(2000, 30000)$

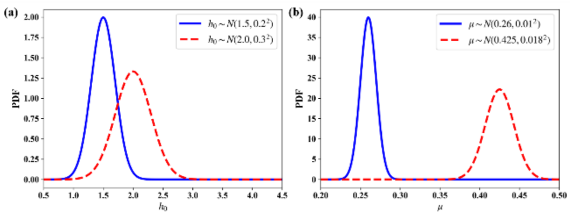

Figure 4: Probabilistic density functions representing uncertainty of (a) h_0 and (b) μ.

Figure 5 shows the PHMs created using the probability distributions listed in Table 1 and threshold h_{cir} = 0.5 m. We first compared them with the PHM to obtained from the uniform distribution case (Fig. 3(b)). During the early winter period, Fig. 5(a), the snow is more slippery, resulting in a wider runout area with probability values close to 1. However, the two periods assuming wet snow show values, Figs. 5(b) and (c), close to 1 in a narrower runout area due to larger friction values. These results are reasonable because dry avalanches reach further than wet avalanches

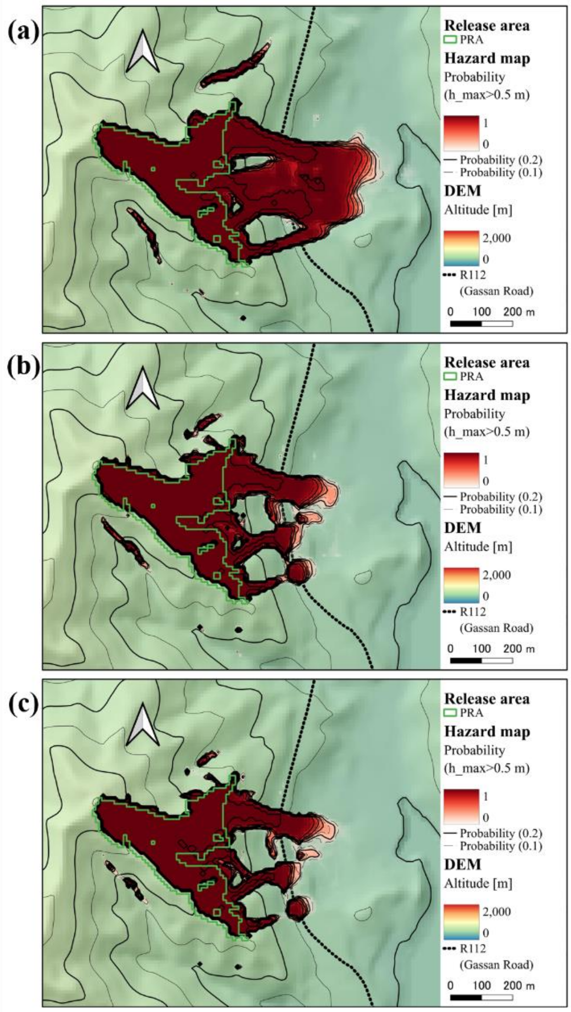

Figure 5: Probabilistic hazard maps using the input variables probability distributions assuming (a) early-winter, (b) mid-winter, and (c) late-winter. Colors represent the exceedance probability of the maximum flow thickness for a threshold of 0.5m

(McClung and Schaerer, 2006; Eckert et al., 2024).

Next, we compared different periods. The early- and late-winter periods, shown in Figs 5(a) and (c) respectively, were given the same h_0-distribution but different μ-distributions. Similar to the uniform case, the runout areas vary significantly. Specifically, the debris reaching the road appears to be discretely distributed in late winter, and their runout seems clearly separated. In the comparison of the two periods with same μ-distribution but different h_0-distributions, Figs 5(b) and (c) respectively, the runout area for mid-winter is slightly larger, but no significant differences are observed. This can be attributed to the large PRA and relatively small 0.5m threshold, which reduces the impact of h_0 on the probability values beyond a certain initial value. Although these results are expected, reflecting the probability distribution of the input variables with real snow conditions (amount and wetness) allows for a more quantitative evaluation of runout areas and their probabilities.

3.4 <u>Validation - Predictability of a Past Avalanche Event</u>

The mid-winter period in this study corresponds to the avalanche event described in Section 2.1. We verified whether PHM could accurately predict an avalanche event. Figure 6 shows the mean value of h_{max} at each location using mid-winter conditions and the runout area of the 2011 avalanche event outlined by the dotted area (Abe et al., 2012). The runout areas exhibited a good agreement.

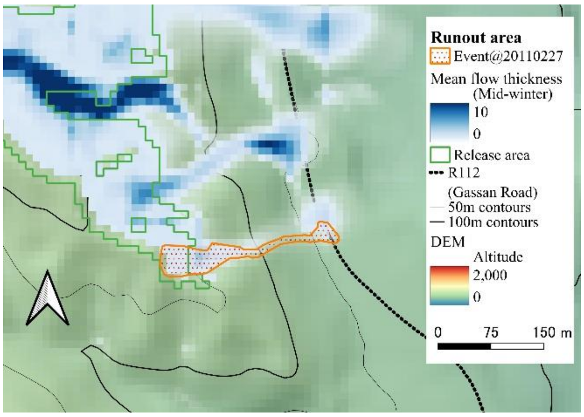

Figure 6: Average flow thickness during the mid-winter period (colors) and the actual avalanche runout area (dotted polygon) as reported by Abe et al. (2012).

In addition to the runout areas, we compared the flow thicknesses on the road. The expected value obtained from the calculations is up to 2.5 m. In contrast, the reported maximum debris height was approximately 5 m (Abe et al., 2012). Although the calculated value was smaller than the reported value, this discrepancy can be attributed to our flow model choice. In this study, snow entrainment effects were ignored.

4. CONCLUSION

In this study, probabilistic hazard maps for snow avalanches that reflect actual snow conditions were prototyped using the PCQ method. First, the PRAs were estimated from topographical conditions. One of the PRAs was selected as the test case, and the PCQ method was implemented to draw the PHM, assuming that the uncertainty of the input values was represented by uniform distributions. Using the obtained polynomial as an emulator, we generated PHMs using input distributions that reflected real snow conditions. These hazard maps show varying runout areas and exceedance probabilities during different periods. Furthermore, this hazard map corresponds well with the runout areas of the past avalanche.

However, the methodology used in the study requires further investigation. For example, the values used for estimating the PRAs were based on the methods proposed in Norway. This needs to be improved through a statistical analysis of the avalanche events that have occurred in Japan. In addition, PRA slopes have high tree and/or avalanche-prevention structures that significantly inhibit the occurrence of avalanches. It is necessary to estimate PRAs while incorporating these effects. Moreover, although a Gaussian distribution was used to represent the uncertainty for each period, it was necessary to establish a method to estimate the distribution of the input variables based on meteorological and snow conditions.

The probabilistic avalanche hazard assessments performed in this study are expected to contribute to risk assessments. Therefore, both exposure and vulnerability must be considered. Exposure to roads can be represented by factors such as the number of passing vehicles and vehicle types (passenger cars, buses, trucks, and others), whereas vulnerability can include vulnerability curves for vehicles and people and the presence of avalanche protection structures. The two types of hazard maps obtained in this study, a map for uniform distributions and maps for non-uniform distributions reflecting the uncertainties of each period, are expected to lead to different risk assessments. The risk assessment from the uniform distribution case represents the risk throughout the winter season for a specific PRA and can help determine the priority of permanent avalanche countermeasures by comparing the risks from different PRAs. By contrast, risk assessment considering the uncertainties of each period represents the daily risk and can inform decision-making for soft countermeasures against urgent avalanches.

It is important to note that the probabilities in this study indicate the likelihood that an avalanche exceeding a given threshold will reach a specific area if it occurs in the PRA. They do not indicate the probability of avalanche occurrence. Avalanche occurrence must be predicted using other methods, such as detecting weak layers within the snowpack using SNOWPACK (Lehning et al., 2004; Mayer et al., 2023). The location of the weak layer will also determine the possible initial flow thickness range. The Incorporation of these methods is expected to yield more user-friendly hazard maps.

ACKNOWLEDGEMENT

This study was funded by JSPS KAKENHI Grant Numbers JP24K17489 to TT, JP22K03747 to KN and TT, and JP21H04601 (HaMaNAS PJ) to KN.

REFERENCES

Abe, O., Nemote, M., Mochizuki, S., Kosugi, K., Hanaoka, M., Machida, M., Machida, T., Abe, T., Kamiishi, I., Hirashima, H.: Observations of the Avalanche Accident Occurred in Route 112 and Judgement of Avalanche Safety for the Surrounding Slopes, Natural Disaster Research Report of the National Research Institute for Earth Science and Disaster Resilience, 47, 71-82, https://dil-opac.bosai.go.jp/publication/nied_natural_disaster/pdf/47/47-07.pdf, 2012. (written in Japanese with English captions)

Bakkehøi, S., Domaas, U., and Lied, K.: Calculation of snow avalanche runout distance. Annals of Glaciology, 4, 24–29. https://doi.org/10.3189/S0260305500005188, 1983.

Barbolini, M., and Savi, F.: Estimate of uncertainties in avalanche hazard mapping. Annals of Glaciology, 32, 299–305. https://doi.org/10.3189/172756401781819373, 2001.

Bühler, Y., Bebi, P., Christen, M., Margreth, S., Stoffel, L., Stoffel, A., Marty, C., Schmucki, G., Caviezel, A., Kühne, R., Wohlwend, S., and Bartelt, P.: Automated avalanche hazard indication mapping on a statewide scale. Natural Hazards and Earth System Sciences, 22(6), 1825–1843. https://doi.org/10.5194/nhess-22-1825-2022, 2022.

Bühler, Y., von Rickenbach, D., Stoffel, A., Margreth, S., Stoffel, L., and Christen, M.: Automated snow avalanche release area delineation – validation of existing algorithms and proposition of a new object-based approach for large scale hazard indication mapping. Natural Hazards and Earth System Sciences, 18(12), 3235–3251. https://doi.org/10.5194/nhess-18-3235-2018, 2018.

Dalbey, K., Patra, A. K., Pitman, E. B., Bursik, M. I., and Sheridan, M. F.: Input uncertainty propagation methods and hazard mapping of geophysical mass flows. Journal of Geophysical Research: Solid Earth, 113(5), 1–16. https://doi.org/10.1029/2006JB004471, 2008.

Derron, M.-H., and Sletten, K.: Method for the susceptibility mapping of snow avalanches in Norway (Tech. Rep.). Geological Survey of Norway, 2016.

Eckert, N., Corona, C., Giacona, F., Gaume, J., Mayer, S., van Herwijnen, A., Hagenmuller, P., and Stoffel, M.: Climate change impacts on snow avalanche activity and related risks. Nature Reviews Earth and Environment, 5, 369–389. https://doi.org/10.1038/s43017-024-00540-2, 2024.

Fischer, J. T., Kofler, A., Fellin, W., Granig, M., and Kleemayr, K.: Multi-variate parameter optimization for computational snow avalanche simulation. Journal of Glaciology, 61(229), 875–888. https://doi.org/10.3189/2015JoG14J168, 2015.

Fischer, J. T., Kofler, A., Huber, A., Fellin, W., Mergili, M., and Oberguggenberger, M.: Bayesian inference in snow avalanche simulation with r.avaflow. Geosciences (Switzerland), 10(5), 191. https://doi.org/10.3390/geosciences10050191, 2020.

Gauer, P.: Avalanche probability: slab release and the effect of forest cover. Proceedings of the International Snow Science Workshop, Innsbruck, Austria, 2018, 76–83, 2018.

Geospatial Information Authority of Japan. (2023). https://www.gsi.go.jp/ENGLISH/index.html (Last accessed: 5th August, 2024)

Heredia, M. B., Prieur, C., and Eckert, N.: Nonparametric estimation of aggregated Sobol' indices: Application to a depth averaged snow avalanche model. Reliability Engineering and System Safety, 212, 107422. https://doi.org/10.1016/j.ress.2020.107422, 2021.

Issler, D., Gisnås, K. G., Gauer, P., Glimsdal, S., Domaas, U., and Sverdrup-Thygeson, K.: Naksin – a New Approach to Snow Avalanche Hazard Indication Mapping in Norway. Available at SSRN: https://ssrn.com/abstract=4530311, 2023.

Lehning, M., Fierz, C., Brown, B., and Jamieson, B.: Modeling snow instability with the snow-cover model snowpack. Annals of Glaciology, 38, 331–338. https://doi.org/10.3189/172756404781815220, 2004.

Mayer, S. I., Techel, F., Schweizer, J., and van Herwijnen, A.: Prediction of natural dry-snow avalanche activity using physics-based snowpack simulations. Natural Hazards and Earth System Sciences, 23, 3445–3465. https://doi.org/10.5194/nhess-23-3445-2023, 2023.

McClung, D. M. and P. A. Schaerer: The Avalanche Handbook. 3rd ed, The Mountaineers, 347 pp. 2006.

Ortner, G., Bründl, M., Kropf, C. M., Röösli, T., Bühler, Y., and Bresch, D. N.: Large-scale risk assessment on snow avalanche hazard in alpine regions. Natural Hazards and Earth System Sciences, 23(6), 2089–2110. https://doi.org/10.5194/nhess-23-2089-2023, 2023.

Rauter, M., Kofler, A., Huber, A., and Fellin, W.: faSavageHutterFOAM 1.0: Depth-integrated simulation of dense snow avalanches on natural terrain with OpenFOAM. Geoscientific Model Development, 11(7), 2923–2939. https://doi.org/10.5194/gmd-11-2923-2018, 2018.

Rauter, M., and Tuković, Ž.: A finite area scheme for shallow granular flows on three-dimensional surfaces. Computers and Fluids, 166, 184–199. https://doi.org/10.1016/j.compfluid.2018.02.017, 2018.

Savage, S. B., and Hutter, K.: The motion of a finite mass of granular material down a rough incline. Journal of Fluid Mechanics, 199, 177–215. https://doi.org/10.1017/S0022112089000340, 1989.

Savage, S. B., and Hutter, K.: The dynamics of avalanches of granular materials from initiation to runout. part i: Analysis. Acta Mechanica, 86, 201–223. https://doi.org/10.1007/BF01175958, 1991.

Sullivan, T. J.: Orthogonal polynomials and applications. In Introduction to Uncertainty Quantification. Texts in Applied Mathematics (vol 63). Springer International Publishing, Cham. https://doi.org/10.1007/978-3-319-23395-6_8, 2015.

Tanabe T., Tsunematsu, K., and Nishimura, K.: Quantitative evaluation of probabilistic hazard mapping with polynomial chaos quadrature and its practical application. ESS Open Archive. https://essopenarchive.org/doi/full/10.22541/essoar.172345615.51028798/v1, 2024.

Tierz, P., Stefanescu, E. R., Sandri, L., Sulpizio, R., Valentine, G. A., Marzocchi, W., and Patra, A. K.: Towards Quantitative Volcanic Risk of Pyroclastic Density Currents: Probabilistic Hazard Curves and Maps Around Somma-Vesuvius (Italy). Journal of Geophysical Research: Solid Earth, 123(8), 6299–6317. https://doi.org/10.1029/2017JB015383, 2018.

Wiener, N.: The Homogeneous Chaos. American Journal of Mathematics, 60(4), 897–936. https://doi.org/10.2307/2371268, 1938.

Xiu, D., and Karniadakis, G. E.: The Wiener–Askey polynomial chaos for stochastic differential equations. SIAM Journal on Scientific Computing, 24(2), 619–644. https://doi.org/10.1137/S1064827501387826, 2002.